

# Mechanically Assisted Solid-State Mixing and Spark Plasma Sintering for Fabrication of Bulk Nanocomposite (WC/7(10Co/4Cr))-Based ZrO<sub>2</sub> Systems

M. Sherif El-Eskandarany, Abdulsalam Al-Hazza, and L.A. Al-Hajji

(Submitted September 9, 2016; in revised form December 21, 2016; published online March 1, 2017)

Mechanically induced solid-state mixing, using high-energy ball milling technique, was employed for preparing WC/7 wt.% (10Cr/4Cr) solid-solution powders. The solid-solution powders obtained after 50 h of milling were mechanically mixed for 50 h together with small weight fractions (0–7 wt.%) of (ZrO<sub>2</sub> + 1.5 wt.% Y<sub>2</sub>O<sub>3</sub>) powders. The powders were then consolidated in vacuum under a uniaxial pressure of 30 MPa at 1250 °C, using spark plasma sintering. The consolidated bulk samples were nearly full dense and maintained their nanocrystalline structure after this consolidation step. The results showed that the consolidated samples over the entire range of ZrO<sub>2</sub> concentrations (0–7 wt.%) had low values for Young's modulus (297–318 GPa) due to their nanocrystalline structures. Moreover, the WC/7 wt.% (10Cr/4Cr)/7(ZrO<sub>2</sub>-1.5 mol.% Y<sub>2</sub>O<sub>3</sub>) showed excellent wear resistance, indexed by its low-value friction coefficient (~0.29).

**Keywords** fracture toughness, mechanical ball milling, nanoindentations, nanotechnology, powder technology

## 1. Introduction

Mechanical alloying (MA) (Ref 1) and mechanical milling (MM) (Ref 2) techniques, using high-energy ball milling method, have been widely employed in fabricating different metastable phases, including nanostructured materials (Ref 3). The fabrication of nanocomposite materials via high-energy ball milling dates back to 1998 when El-Eskandarany (Ref 4) used this method to prepare homogeneous SiC<sub>p</sub>/Al nanocomposite powders with high volume fractions (25%) of SiC nanoreinforcement particles. Cemented carbides (Ref 5, 6) such as tungsten carbide-cobalt composites are characterized by extraordinary hardness and wear resistance resulting from the high carbide content (Ref 7). This class of materials has been widely used as cutting tools and wear-resistant components due to the singular combination of their properties, including high hardness, moderate toughness and excellent wear resistance. WC has a high melting point of approximately 2900 °C, which impedes bulk preparation of dense pure WC using conventional sintering techniques (Ref 8). Addition of metal Co binder to WC improves the sintering and increases the strength and toughness; however, the hardness and wear resistance of the cemented carbides are significantly reduced. Moreover, the composites containing such metallic binders are inferior to WC in terms of corrosion and elevated temperature applications

(Ref 9, 10). All of these factors limit the applications of the WC-metal binder composites.

In 2000, El-Eskandarany replaced the traditional metal Co binder with a nonmetal-binder nanocrystalline MgO material (Ref 11) to fabricate fully dense bulk nanocomposites that exhibited excellent mechanical properties. Since then, nanocrystalline Al<sub>2</sub>O<sub>3</sub> (Ref 12) and ZrO<sub>2</sub> (Ref 13) have been used as nonmetal binders to extend the life of WC materials and to improve their mechanical and physical properties.

The present work aims to study the effect of adding small concentrations (0–7 wt.%) of ZrO<sub>2</sub>-1.5 wt.% Y<sub>2</sub>O<sub>3</sub> nanocrystalline powders on improving the fracture toughness and wear resistance of mechanically mixed 93WC/7(10Co/4Cr) nanocomposite powders. The selection of ZrO<sub>2</sub> was based on the fact that it has a high thermal stability and excellent mechanical properties, such as high bending strength and excellent fracture toughness (Ref 14).

## 2. Experimental Procedure

### 2.1 Preparation of the WC Nanocrystalline Powders

A 15-g sample of commercial WC powder (99.9%, 200 μm) was balanced and charged into a WC vial (45 ml in volume) and sealed together with 5 WC balls (10 mm in diameter) in a glove box (UNILAB Pro Glove Box Workstation, mBRAUN, Germany) under an helium gas atmosphere. The milling process was carried out for 20 h at room temperature using a high-energy mixer ball mill (SPEX 8000-D Mixer/Mill, USA). However, the ball milling process was interrupted after selected milling time (0, 3, 15 h) to take samples for investigations, and the microstructure and grain size change with changing the milling time. The long-term milling procedure (20 h) was repeated 25 times in order to obtain approximately 350 g of ultrafine nanocrystalline WC powder for the preparation of WC-based nanocomposite materials.

M. Sherif El-Eskandarany, Abdulsalam Al-Hazza, and L.A. Al-Hajji, Nanotechnology and Advanced Materials Program, Energy and Building Research Center, Kuwait Institute for Scientific Research, 13109 Kuwait, State of Kuwait. Contact e-mail: msherif99@yahoo.com.

## 2.2 Preparations of the Nanocomposite 93WC/7(10Co/4Cr) Powders

The as-ball-milled WC nanocrystalline powders obtained after 20 h of ball milling were mixed with elemental Co (99.99%, 10  $\mu\text{m}$ ) and Cr (99.99%, 150  $\mu\text{m}$ ) in the glove box under helium gas atmosphere to give the starting nominal composition (wt.%) of 93WC/7(10Co/4Cr). The mixed powders were then charged into WC vial (250 ml in volume) together with 25 WC balls (10 mm in diameter) to give a ball-to-powder weight ratio as 20:1. The ball milling procedure was carried out at room temperature for 50 h, using a Fritsch P5 high-energy ball mill (Germany) at a rotation speed of 250 rpm. In order to investigate the effect of milling time on the elemental distribution and particle size of the composite powders, the process was stopped after 6, 12.5, 25 h of the milling time and the vials were opened in the glove box to take represented samples.

## 2.3 Preparations of the Nanocomposite 100-x(93WC/7(10Co/4Cr))/x(ZrO<sub>2</sub>-1.5 mol.% Y<sub>2</sub>O<sub>3</sub>) Powders

The as-prepared 93WC/7(10Co/4Cr) composite powders obtained after 50 h of ball milling were simply mixed in the

glove box with different wt.% (x) of (ZrO<sub>2</sub>-1.5 mol.% Y<sub>2</sub>O<sub>3</sub>) powders to yield the desired nominal composition of x (0, 1, 2, 3, 4, 5, 7, and 7 wt.%) and then charged into the WC vial and sealed together with 25 WC balls. The vials were then mounted on the high-energy ball mill where the milling process conducted with a rotation speed of 250 rpm for 50 h. Selected samples were taken after milling for 0, 6, 12.5, and 25 h for characterizations.

## 2.4 Powder Consolidation

To take the advantage of the unique properties of the synthesized nanocomposite powders, the consolidation procedure using spark plasma sintering (SPS) was a necessary step to conduct a reliable investigation of the bulk properties of the fabricated materials. To consolidate the nanocomposite powders into the perfect cylindrical shapes with 20 mm in diameter and 20 mm in height, the powders were first dried in a vacuum oven at 150 °C for 24 h. The activated powders were then gently ground using agate mortar and pestle inside a glove box filled with helium atmosphere. The powders with different ZrO<sub>2</sub>-2 mol.% Y<sub>2</sub>O<sub>3</sub> concentrations (x) were individually consolidated into bulk samples using the graphite mold SPS system (SPS-825, Fuji Electronic Industrial Co., Ltd, Japan).

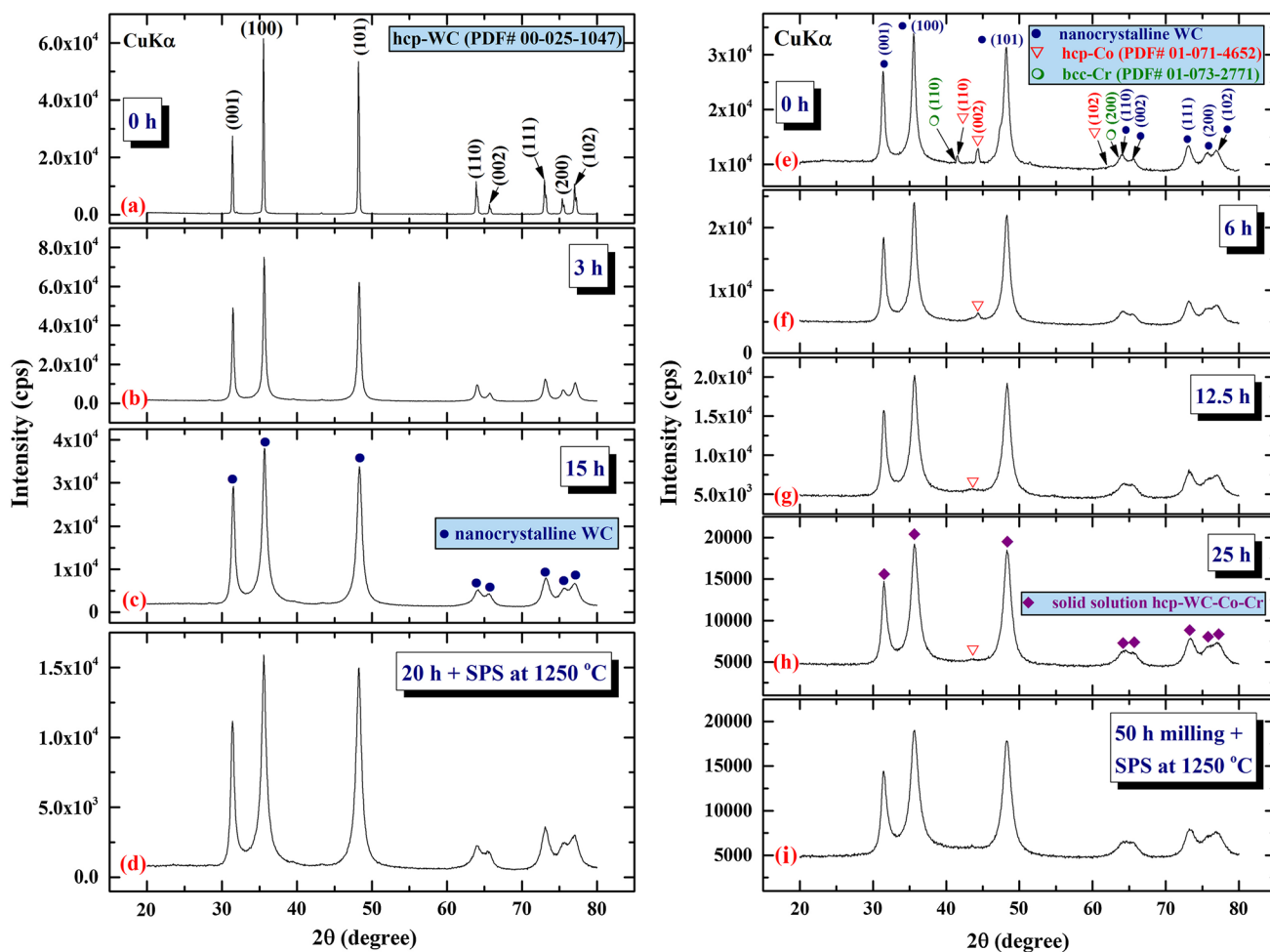


**Fig. 1** XRD patterns of as-received hcp-WC powders after mechanical milling time for (a) 0, (b) 3, and (c) 15 h. The XRD pattern of the powders milled for 20 h and then consolidated at 1250 °C, using SPS technique, is presented in (d). The XRD patterns of as-mechanically milled WC powders and then ball milled with 7 wt.% of (10Co/4Cr) powders for 0, 6, 12.5, and 25 h are shown in (e-h), respectively. The XRD pattern of 93-WC/7 wt.% (10Co/4Cr) powders obtained after 50 h and then consolidated at 1250 °C, using SPS technique, is presented in (i)

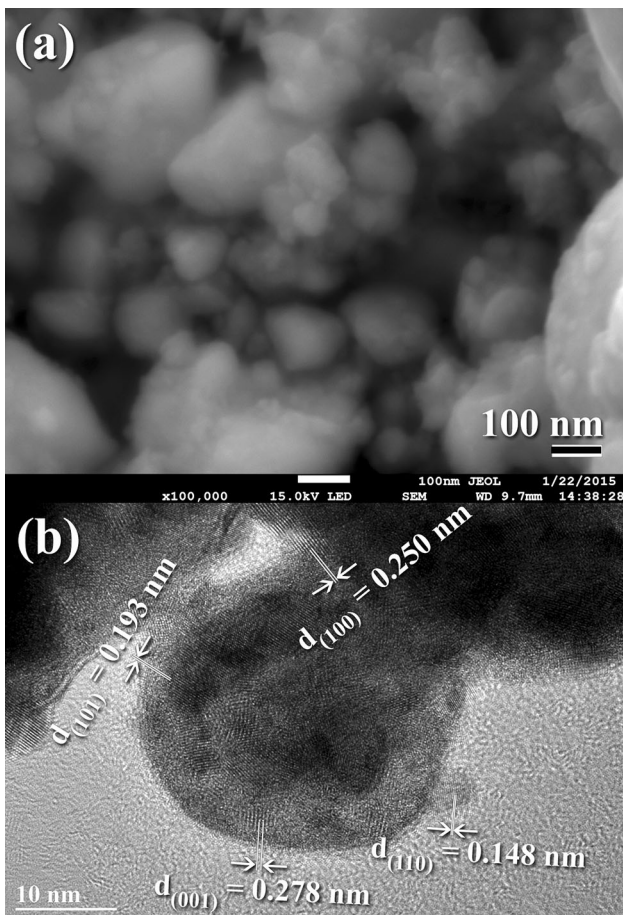


**Fig. 2** (a) FE-SEM micrograph, and (b) HRTEM image of as-mechanically ball-milled hcp-WC for 20 h

The consolidation procedure was performed under vacuum at 1250 °C with an applied uniaxial pressure of 30 MPa. To avoid any undesired grain growth, the sintering process was applied for only 3 min, and no binding materials were added. Further experimental details for the SPS process are discussed elsewhere (Ref 9, 10).

### 2.5 Sample Characterization

Total structural investigations of the nanocomposite powders with different ZrO<sub>2</sub>-1.5 mol.% Y<sub>2</sub>O<sub>3</sub> concentrations were performed via powder x-ray diffraction (XRD) using Rigaku-Smart Lab 9 kW equipment. A high-speed 1D x-ray detector D/teX Ultra 1D mode (D/teX) with a Ni filter was used. All of the samples were analyzed at a rate of 2 degree/min in continuous 2θ/θ scan mode using CuKα radiation (λ = 0.15418 nm) at 45 kV and 200 mA. The diffraction patterns were obtained over the 2θ range of 20°-80°, with a step size of 0.02 degree 2θ and a time of 1 s/step.

A 200-kV field-emission high-resolution transmission electron microscopy (FE-HRTEM), JEOL-2100F, Japan, was used to investigate the local structure of as-synthesized nanocomposite powders. The energy-dispersive x-ray spectroscopy (EDS), using FE-HRTEM scanning transmission electron microscopy (STEM) system, was carried out to determine the local composition of the ball-milled powders. The morphology of the synthesized nanocomposite powders and their corre-

sponding bulk materials were examined by field-emission scanning electron microscopy (FE-SEM) in conjunction with energy-dispersive x-ray spectroscopy (EDS) using a JEOL JSM-7800F microscope (Japan). The topological and surface properties of the fabricated bulk nanocomposites samples were investigated by contact-mode atomic force microscopy (AFM) using an Agilent 5600LS AFM system (USA).

The hardness of all of the consolidated samples was determined using the Vickers hardness test with a load of 30 kg. In these experiments, the microhardness values were the averages of at least 60 readings obtained for each sample. The fracture toughness of the consolidated samples was determined using the VHT indenter crack-length measurements approach. Nanoindentation was employed to determine the nanomechanical properties of the as-consolidated nanocomposite samples using a Bruker Nanoindenter (Germany) with a diamond Berkovich tip. This technique investigates the values of nanohardness and Young's modulus (modulus of elasticity) of the bulk samples produced in the present work. To accomplish this task, more than 100 indents for each sample were generated using a single-indent continuous multi-cycle ramp approach with an applied force of 400 mN. The density of all bulk samples (as-consolidated samples) was measured by AUTOMATIC TRUE DENSITY ANALYZER (The SEISHIN Enterprise Co., LTD, Japan). The rule-of-mixtures (ASTM Standard D792-00) (Ref 15) approach was used to estimate the theoretical density of the consolidated sample. The relative density was calculated by dividing the measured density of each sample over the corresponding theoretical values.

The tribological behavior of bulk WC/7 wt.% (10Cr/4Cr)/7(ZrO<sub>2</sub>-1.5 mol.% Y<sub>2</sub>O<sub>3</sub>) nanocomposite sample was characterized by a pin-on-disk tribometer (Microtest, S.A, Madrid-Spain) against WC-8Co ball (10 mm in diameter). The sliding speed of the specimen relative to the ball was 150 rpm, and the sliding distance was 700 m, using an applied force of 150 N. The coefficient of friction of the sliding couple was continuously recorded during the test.

## 3. Results and Discussion

The XRD pattern of as-received WC powders is shown in Fig. 1(a). The starting material powders consisted of polycrystalline large crystallites, characterized by sharp Bragg peaks corresponding to hcp-WC phase (PDF# 00-025-1047), as elucidated in Fig. 1(a). When the powders subjected to continuous ball milling for 3 h, significant broadening can be notified in the major ((001), (100), (101)) and minor ((110), (002), (111), (200), (102)) Bragg peaks denoting mechanically induced microstructure refinement, as shown in Fig. 1(b). Increasing the ball milling time (15 h) assisted the continuity of the grain refining, as indicated by outstand broadening in the Bragg peaks displayed in Fig. 1(c). We should emphasize that during this stage of milling, WC powders experienced repeated collision, fracture, and cold welding. Such severe plastic deformation induced by high-energy ball milling lead also to accumulation of internal stresses that changes the lattice parameter and formation of cell structure (Ref 16).

The FE-SEM taken at a magnification of 100,000 and FE-HRTEM micrographs of the end-product of WC powders obtained after 20 h of the mechanical milling (MM) time are shown in Fig. 2(a), (b), respectively. At this final stage of ball

milling, the powders had smooth featured surfaces and became ultrafine with an average apparent diameter of 185 nm, as shown in Fig. 2(a). Moreover, the as-ball-milled nanopowders tended to aggregate due to the Van der Waal force to form larger particles with an average diameter of 413 nm in diameter, as presented in Fig. 2(a). These nanopowder particles consisted of ultrafine grains ranging between 3 and 8 nm in diameter, as shown in Fig. 2(b). The indexed grains in Fig. 2(b) had different orientations related to interplanar spacing ( $d$ ) of 0.520, 0.193, 0.278, and 0.148 nm that well matched with (100), (101), (001) and (110), respectively (PDF# 00-025-1047).

**Table 1** Effect of MM time on the lattice parameters  $a$  and  $c$  of WC milled with 7 wt.% of (10Co/4Cr) powders

MM time, h	Lattice parameter of WC, nm	
	$a$	$c$
0	0.2906**	0.2878**
3	0.2905	0.2879
6	0.2909	0.2882
9	0.2914	0.2887
12.5	0.2919	0.2892
18	0.2924	0.2898
25	0.2929	0.2903
50	0.2931	0.2904

\*Calculated from the major Bragg peak of hcp-WC (100)  
 \*\*PDF Card No. : 00-025-1047

When the nanocrystalline WC powder particles obtained after 20 h of MM time were consolidated at 1250 °C using SPS technique, the materials maintained their nanocrystalline characterizations, suggested by the broadening seen in the hcp-WC Bragg peaks presented in Fig. 1(d). This indicates the formation of bulk nanocrystalline WC material.

These fine WC-nanopowder particles obtained after 20 h of MM time were mixed with 7 wt.% of (10Co/4Cr) powders and then ball milled for different MM time. The XRD pattern of the starting WC/7 wt.%(10Co/4Cr) powders (before ball milling, 0 h) is shown in Fig. 1(e). The powders consisted of nanocrystalline hcp-WC (reinforcement materials) coexisted with large crystalline phases of elemental hcp-Co (PDF# 01-071-4652) and bcc-Cr (PDF# 01-073-2771), as indicated in Fig. 1(e). After MM time ranged between 6 and 25 h, the elemental metallic powders of Co and Cr were subjected to aggressive grain refining caused by the milling media (WC balls) together with the nanomilling media (WC-nanopowders), as indicated by the significant broadening seen in their Bragg peaks shown in Fig. 1(f). During the intermediate (12.5-25 h) stage of MM time, the Bragg diffractions related to the elemental powders of Co and Cr can be hardly seen (Fig. 1g, h), suggesting the formation of solid-solution WC-Co-Cr nanocrystalline phase.

During the ball milling process, the precursor WC, Co, and Cr powders undergone to different mechanical deformation generated by the milling media such as cold welding, fracturing, rewelding and lattice imperfections. Such severe defects led to enhance the diffusion of Co and Cr atoms into the WC matrix and the formation of metastable solid-solution phase. The formation of WC-Co-Cr solid solution is indicated by the significant continuous shifts observed in the Bragg peaks

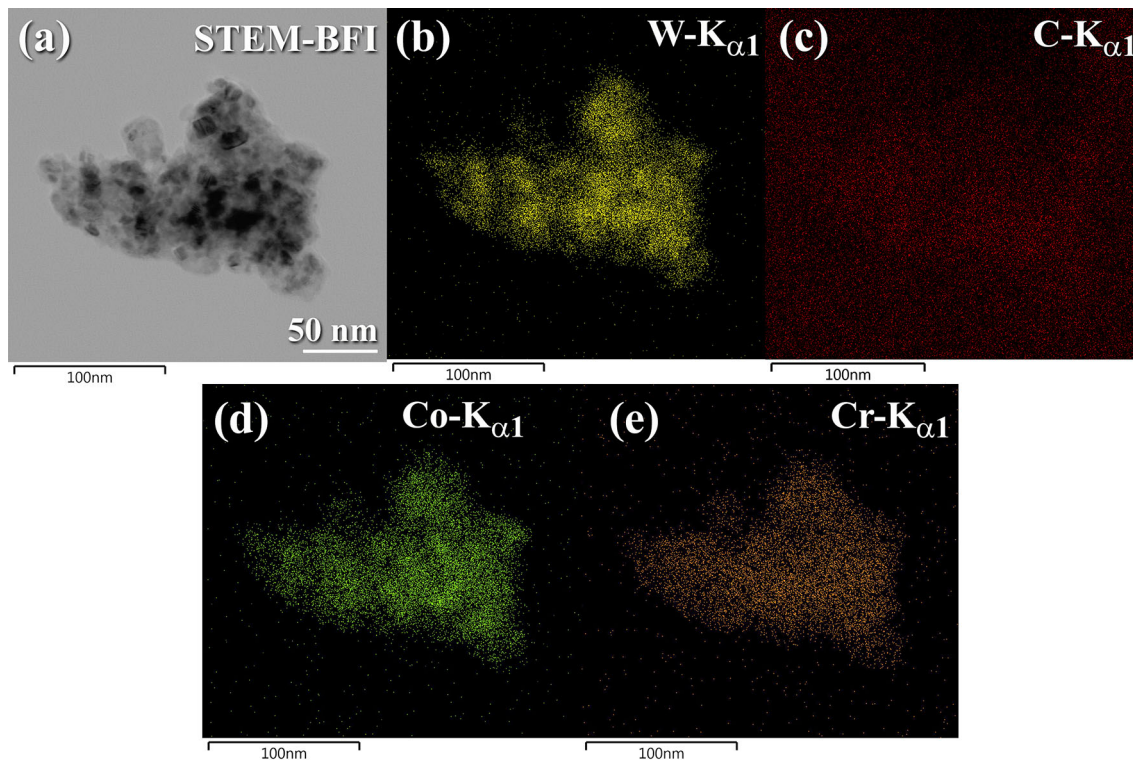


**Fig. 3** (a) STEM-BFI of as-ball-milled WC nanocrystalline powders obtained after 20 h of the milling time and then mechanically mixed with 7 wt.% (10Co/4Cr) powders for 50 h, using a high-energy ball mill. The corresponding x-ray elemental mapping of W- $K_{\alpha 1}$ , C- $K_{\alpha 1}$ , Co- $K_{\alpha 1}$ , and Cr- $K_{\alpha 1}$  is displayed in (b-e), respectively

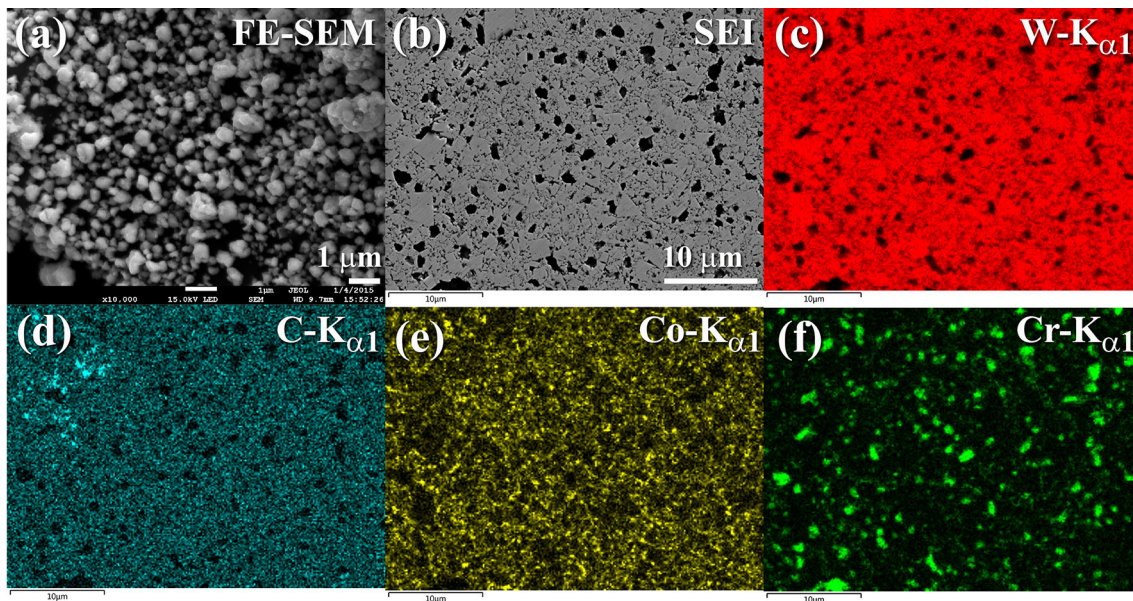


**Fig. 4** (a) FE-SEM of nanocomposite 93-WC/7 (10Co/4Cr) powders obtained after 50 of ball milling time. The cross-sectional view of the consolidated powders achieved at 1250 °C, using SPS technique, is presented in (b) together with the corresponding x-ray elemental mapping of (c) W-K<sub>α1</sub>, (d) C-K<sub>α1</sub>, (e) Co-K<sub>α1</sub>, and (f) Cr-K<sub>α1</sub>

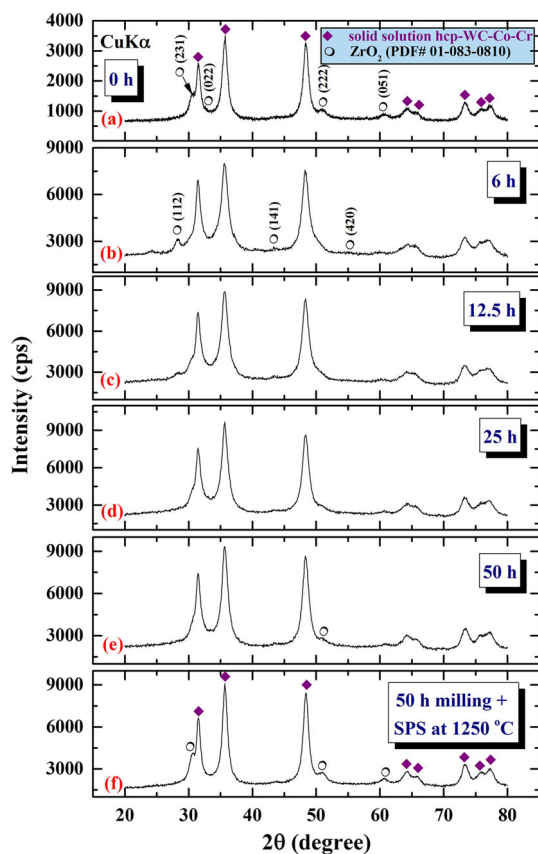


**Fig. 5** XRD patterns of as-mechanically milled 93-WC/7 (10Co/4Cr) powders obtained after 50 h of ball milling time and then mechanically mixed with 7 wt.% (ZrO<sub>2</sub>) powders for (a) 0, (b) 6, (c) 12.5, (d) 25, and (e) 50 h. The XRD pattern of nanocomposite 93(93-WC/7 wt.%(10Co/4Cr))/7 wt.% ZrO<sub>2</sub> powders obtained after 50 h and then consolidated at 1250 °C, using SPS technique, is presented in (f)

of WC to the low-angle side upon increasing milling time from 0 h (Fig. 1e) to 25 h (Fig. 1h). In order to ensure the solubility of Co and Cr metals into the WC lattice and the formation of solid-solution WC-Co-Cr phase, the lattice parameters  $a$  and  $c$  of Bragg peak WC(100) were calculated by using Eq 1 as different ball milling time (Table 1).

$$1/d^2 = (h^2 + k^2)/a^2 + l^2/c^2 \quad (\text{Eq 1})$$

where  $h$ ,  $k$  and  $l$  are miller indices,  $d$  is the atomic lattice spacing, and  $a$  and  $c$  are lattice parameters of hcp-WC. In the early stage of MM time (0-3 h), the both of  $a$  and  $c$  values were very closed to the reported values for WC (PDF Card No.: 00-025-1047), as shown in Table 1. A significant increase in these values was observed during the intermediate stage of MM (3-18 h) suggesting a continuous increase in the number of Co and Cr atoms diffused into the WC lattice. Toward the final stage of MM (18-50 h), both of  $a$  and  $c$  tended to saturated at  $\sim 0.2929$  and  $0.2903$  nm, respectively, implying the completion of the MM process and the formation of solid-solution WC-Co-Cr phase, as elucidated in Table 1.

In order to understand the homogeneity and the elemental distribution of the reinforcement WC nanograins into the matrix of Co/Cr powders, the nanocomposite powders obtained after 50 h of MM time were examined by STEM-EDS elemental mapping (Fig. 3). Fine WC cells with grain sizes ranging between 18 and 27 nm in diameter (Fig. 3a) were uniformly embedded (Fig. 3b, c) into the fine metallic matrix (light gray region in Fig. 3a) of Co (Fig. 3d) and Cr (Fig. 3e) to form homogeneous WC/7 wt.% (10Co/4Cr) nanocomposite powders, as shown in Fig. 3. This homogeneous metastable nanocomposite powders maintained its nanoscaled size and nanocrystallinity without any remarkable grain growth even after consolidation at 1250 °C, using SPS technique (Fig. 1i).

The FE-SEM micrograph of nanocomposite WC/7 wt.%(10Co/4Cr) powders obtained after 50 h of MM time is shown in Fig. 4(a). After this stage of ball milling, the powders

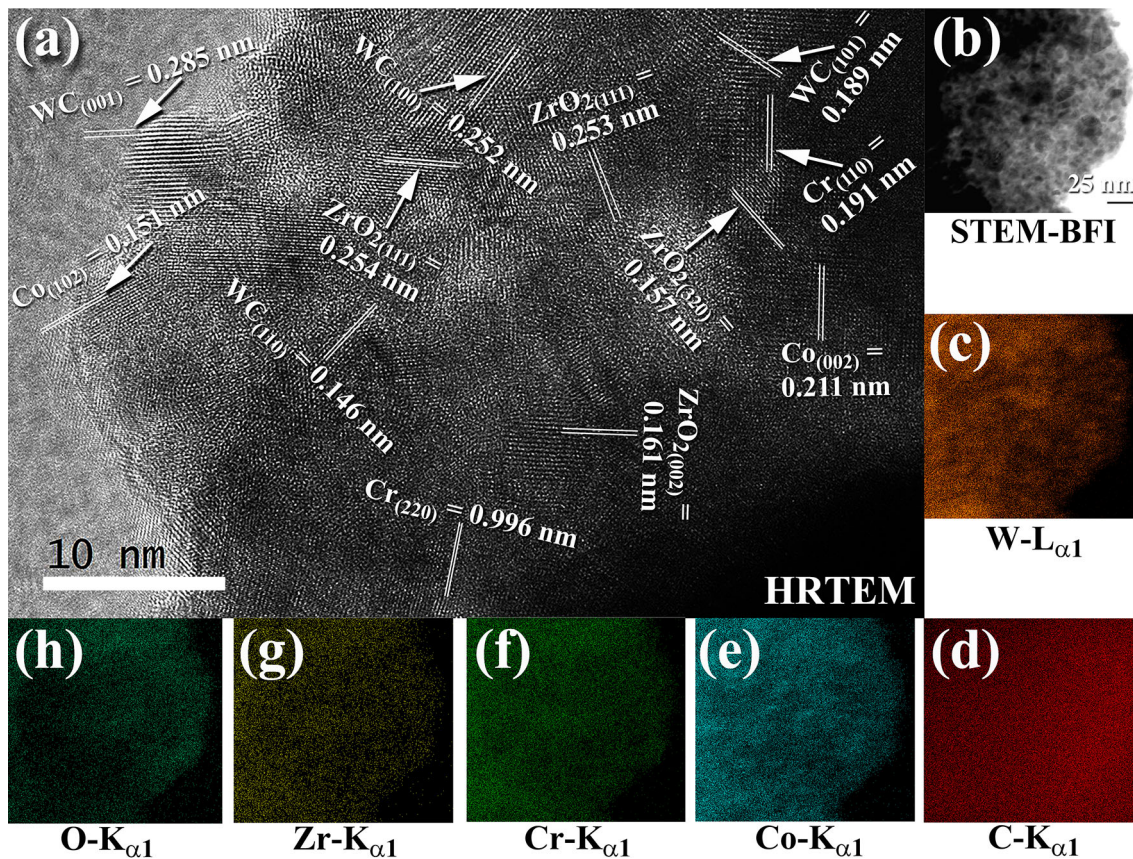


**Fig. 6** (a) HRTEM and (b) STEM-BF images of nanocomposite 93(93-WC/7 wt.% (10Co/4Cr))/7 wt.% ZrO<sub>2</sub> powders obtained after 50 h of the ball milling time. The corresponding x-ray elemental mapping is elucidated for (c) W-L<sub>α1</sub>, (d) C-K<sub>α1</sub>, (e) Co-K<sub>α1</sub>, (f) Cr, (g) Zr-K<sub>α1</sub> and (h) O-K<sub>α1</sub>

had spherical-like morphology with particle size in the range between 0.35 and 1.2 μm in diameter, as displayed in Fig. 4(a). This sample showed slight grain growth upon consolidation at 1250 °C by SPS, as indicated in Fig. 4(b). The nanocomposite materials obtained upon SPS technique had excellent homogeneous distribution of the sharp angular fine grain (less than 5 μm in diameter) related to the WC (Fig. 4b-d) into the metallic matrix of Co (Fig. 4(e) and Cr (Fig. 4(f). Neither pores nor reinforcement-free zones were existed in the as-consolidated powders, suggesting the formation of a uniform bulk WC/6 wt.%(10Co/4Cr) nanocomposite material (Fig. 4).

The as-mechanically milled 93-WC/7 wt.% (10Co/4Cr) nanocomposite powders obtained after 50 h of ball milling time were then mechanically mixed with 7 wt.% (ZrO<sub>2</sub>/1.5 wt.% Y<sub>2</sub>O<sub>3</sub>) for different MM time. At the starting stage (0 h) the powders consisted of solid-solution hcp-WC-Co-Cr coexisted with large crystalline grains of ZrO<sub>2</sub> (PDF# 01-083-0810), as shown in Fig. 5(a). Those Bragg reflections related to ZrO<sub>2</sub> tended to have clear broadening with decrease in their intensities upon increasing the MM time between 6 h (Fig. 5b) and 12.5 h (Fig. 5c). This suggests the diffusion of ZrO<sub>2</sub> phase into the hcp-WC-Co-Cr matrix. The Bragg peaks related to ZrO<sub>2</sub> phase were hardly detected when the MM time increased in the range between 25 h (Fig. 5d) and 50 h (Fig. 5e), suggesting the formation of metastable hcp-93(93-WC/7 wt.%(10Co/4Cr))/7 wt.% ZrO<sub>2</sub> powders.

The HRTEM image of 93(93-WC/7 wt.% (10Co/4Cr))/7 wt.% ZrO<sub>2</sub> powders obtained after 50 h of MM time is shown

in Fig. 6(a). The sample consisted of numerous fine grains (5–10 nm in diameter) of WC, Co, Cr, and ZrO<sub>2</sub> with different orientation, as indexed in Fig. 6(a). The morphological characterization of this sample examined by STEM-bright field image, BFI (Fig. 6b) and corresponding x-ray EDS mapping (Fig. 6c-h) indicated that the ultrafine WC grains (~8–20 nm in diameter, Fig. 6b–d) having lens-like morphology (Fig. 6b) were uniformly distributed into the light gray matrix of Co (Fig. 6e)/Cr (Fig. 6f)/ZrO<sub>2</sub> (Fig. 6g, h) to form a partially solid-solution phase. This formed metastable solid-solution phase tended to be dissociated into hcp-WC-Co-Cr coexisted with ZrO<sub>2</sub> upon SPS consolidation procedure at 1250 °C, as indexed by the appearance of the Bragg peaks related to ZrO<sub>2</sub> phase shown in Fig. 5(f).

The FE-SEM micrograph of the cross-sectional view for 93(93-WC/7 wt.%(10Co/4Cr))/7 wt.% ZrO<sub>2</sub> powders obtained after 50 h of MM time and then consolidated into bulk material at 1250 °C, using SPS, is shown in Fig. 7(a). In general, the composite material had fine structure containing micro-grained WC embedded into the Co/Cr matrix reinforced by ZrO<sub>2</sub> (Fig. 7a). The high-magnification FE-SEM micrograph of the indexed region in Fig. 7(a) is shown in Fig. 7(b). The consolidated sample was dense with no remarkable pores or cavities. In addition, the WC grains (light gray grains) did not suffer from drastic growth upon consolidation, indicated by their fine grain sizes characterizations (ranging between 260 and 887 nm in diameter), as presented in Fig. 7(b). It can be notified that the black matrix zone (Fig. 7b) consisting of Co

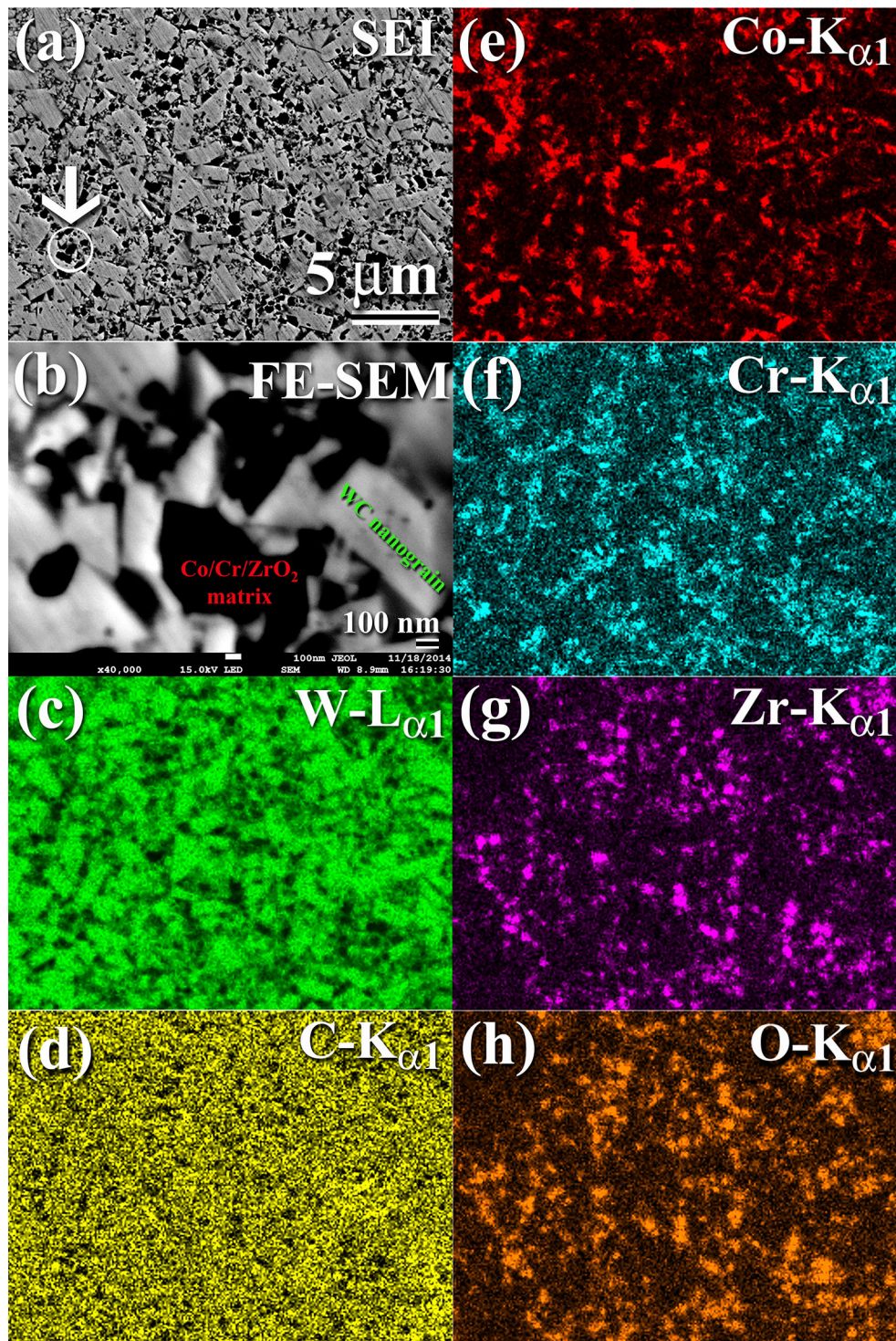


**Fig. 7** (a) FE-SEM micrograph of the cross-sectional view of as-ball-milled nanocomposite 93(93-WC/7 wt.%(10Co/4Cr))/7 wt.% ZrO<sub>2</sub> powders (50 h) and then consolidated at 1250 °C, using SPS technique. The high magnification ( $\times 40,000$ ) for the zone indexed by a circular symbol shown in (a) is presented in (b). The x-ray elemental mapping corresponding to (a) is shown in the figure for (c) W-L <sub>$\alpha$ 1</sub>, (d) C-K <sub>$\alpha$ 1</sub>, (e) Co-K <sub>$\alpha$ 1</sub>, (f) Cr-K <sub>$\alpha$ 1</sub>, (g) Zr-K <sub>$\alpha$ 1</sub>, and (h) O-K <sub>$\alpha$ 1</sub>

(Fig. 7e) and Cr (Fig. 7f) was reinforced by ZrO<sub>2</sub> fine nanopowder particles (Fig. 7g, h). The existence of such a hard ZrO<sub>2</sub> particles into the metallic matrix may act as grain growth inhibitors for WC grains (Fig. 7c, d) to maintain their nanocrystalline characterizations.

The theoretical bulk densities for the nanocomposite 100-x(93-WC/7(10Co/4Cr))/x ZrO<sub>2</sub> were calculated at different

ZrO<sub>2</sub> concentrations (x) using the rule of mixtures (Ref 15) and are plotted in Fig. 8 along with the measured and relative densities. All of the consolidated samples had relative densities higher than 99.95%, implying a full densification process that minimized the pore fractions in the consolidated samples. It can also be inferred from the figure that increasing the volume fraction of ZrO<sub>2</sub> leads to a monotonical decrease in the bulk

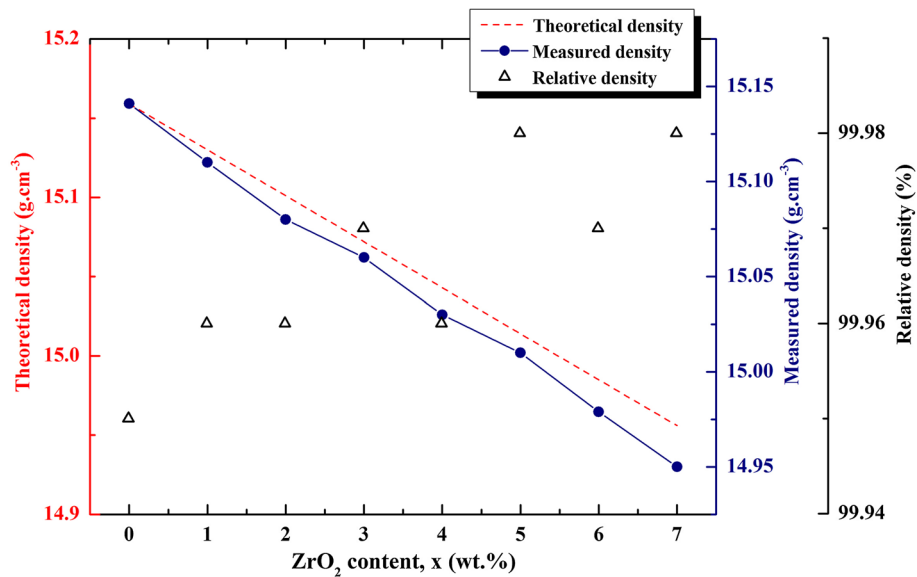


**Fig. 8** Calculated theoretical (broken line), measured (closed symbols) and relative densities (open symbols) of the bulk 93(93-WC/7 wt.%(10Co/4Cr)) mixed with different ZrO<sub>2</sub> contents, x

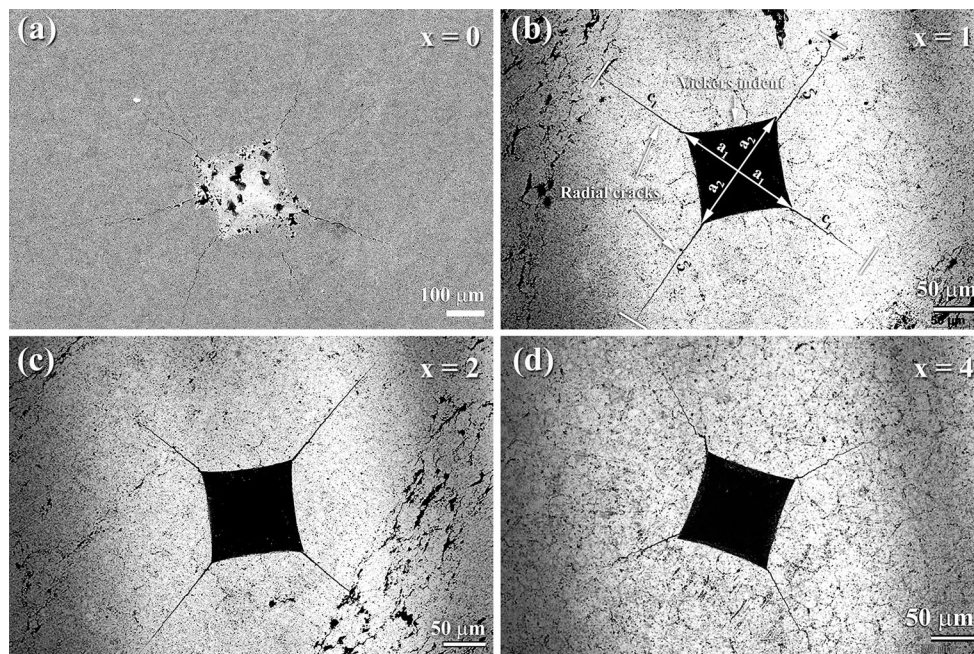


**Fig. 9** Optical micrographs of the Vickers indents (HV30) for the bulk 100-x (93-WC/7 wt.%(10Co/4Cr)) nanocomposites with ZrO<sub>2</sub>, x concentrations of (a) 0, (b) 1, (c) 2 and (d) 4 wt.%

density of the nanocomposites. This is a natural consequence of replacing the high-density WC, metallic Co and Cr fractions with ZrO<sub>2</sub> phase.

The optical micrographs from the Vickers hardness indentation for the consolidated samples with different ZrO<sub>2</sub> concentrations (x) are shown in Fig. 9. The cracks around the Vickers indents present in all of the micrographs shown in Fig. 9 were developed after the indentation procedure. The average length of these cracks for each sample was used to estimate the fracture toughness ( $K_{C1}$ ) using the model proposed by Anstis et al. (Ref 17-19). The crack lengths decreased upon

increasing the ZrO<sub>2</sub> and suggested a monotonical increase in  $K_{C1}$  with increasing x, as shown in Fig. 9.

The FE-SEM micrograph of the bulk 93(93-WC/7 wt.%(10Co/4Cr))/7 wt.% ZrO<sub>2</sub> sample after the Vickers hardness test is shown in Fig. 10(a). The average length of the cracks demonstrated in the figure extended up to 74.8 μm from the indent, which indicates a  $K_{C1}$  value of 15.48 MPa m<sup>1/2</sup>. The multi-indentations presented in Fig. 10(b) have nearly the same dimensions, indicating the homogeneity in composition and nanomechanical properties of the bulk 100-x(93-WC/7 wt.%(10Co/4Cr))/x ZrO<sub>2</sub> nanocomposite materials. The AFM



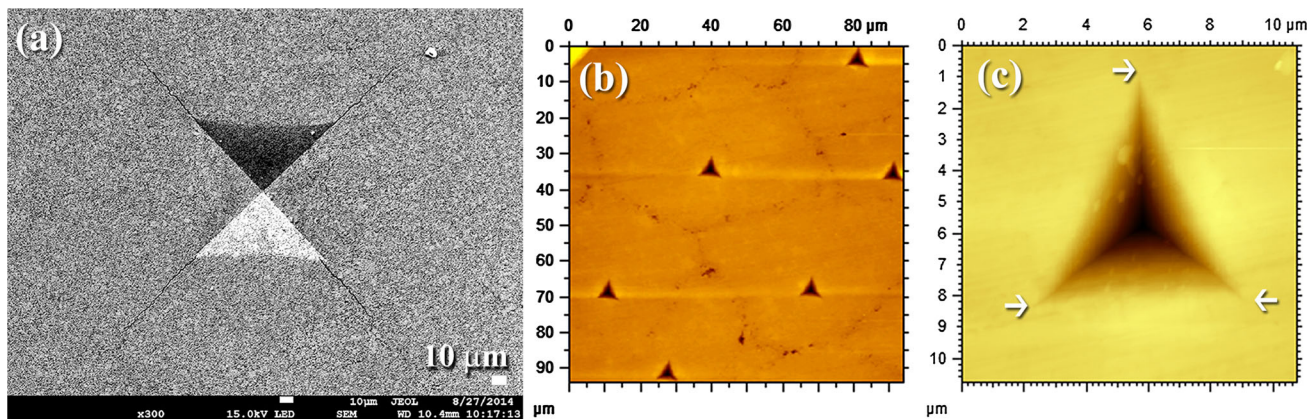


**Fig. 10** (a) FE-SEM micrograph of a single Vickers indent (HV30) and (b) AFM image of selected nanoindents developed on the surface of the bulk 93(93-WC/7 wt.%(10Co/4Cr))/7 wt.% ZrO<sub>2</sub> nanocomposite. Micro- and nanoradial cracks around the indents are perceived in (a) and (c), respectively

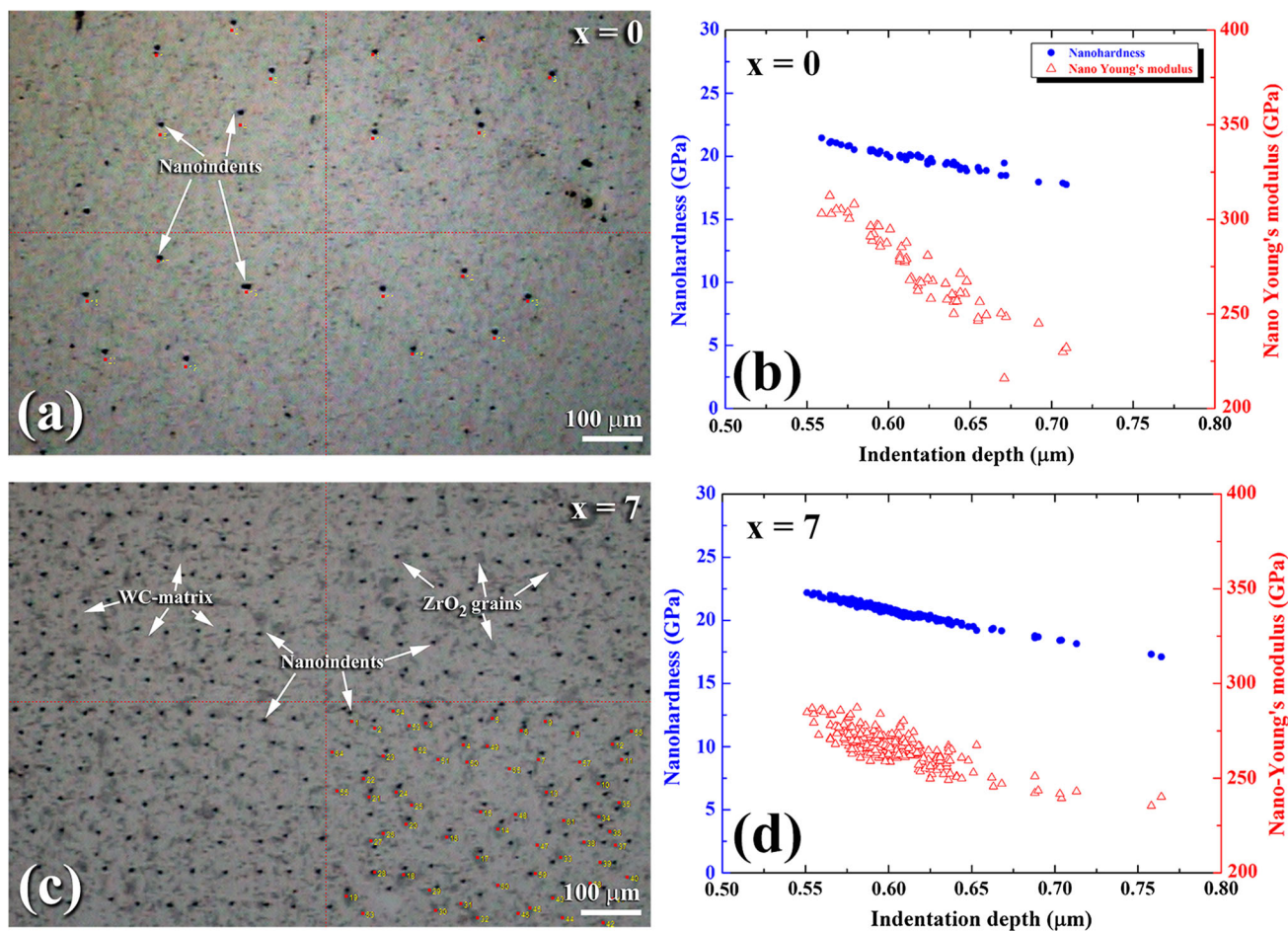


**Fig. 11** Optical micrographs of the planar cross-sectional view of the as-consolidated (a) 93WC/7(10Co/4Cr) and (c) 93(93-WC/7 (10Co/4Cr))/7 ZrO<sub>2</sub> samples, showing Berkovich indents in various examined zones. The corresponding nanoindentations and nano-Young's modulus are shown in (b) and (d), respectively

micrograph of a single nanoindent taken at a higher magnification shows radial cracks around the nanoindent with ductile fracture, as presented in Fig. 10(c). The absence of sink-in behavior from the fractured surface can be seen. Sinking-in is expected in materials that exhibit a low value of  $E/Y$  (where  $E$  is the Young's modulus, and  $Y$  is the yield strength) (Ref 20).

Figure 11 shows the optical micrographs of the cross-sectional view of the consolidated samples of 93WC/7(10Co/4Cr) (a) and 93(93-WC/7 (10Co/4Cr))/7 ZrO<sub>2</sub> (c). The relationships between nanohardness, nano-Young's modulus and the indentation depth of the examined samples are presented in (b) and (d) for 93WC/7(10Co/4Cr) and 93(93-

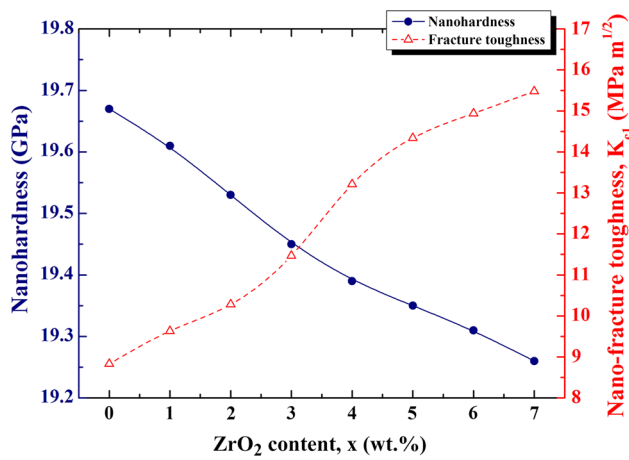


**Fig. 12** Dependence of nanohardness and fracture toughness on the ZrO<sub>2</sub> content for bulk nanocomposite 100-x(93-WC/7(10Co/4Cr))/x ZrO<sub>2</sub> materials

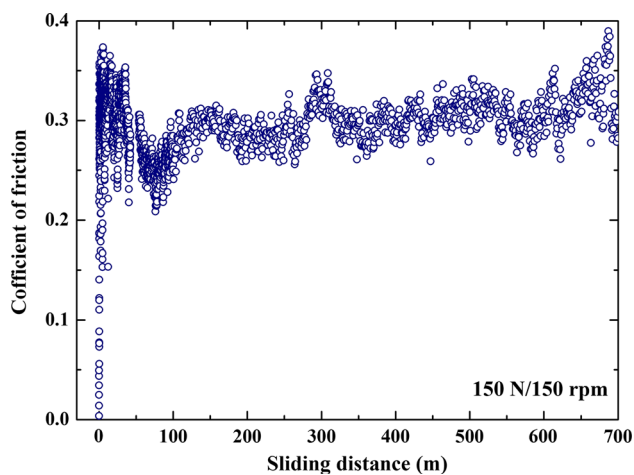


**Fig. 13** Dynamic coefficient of friction curve for bulk WC/7wt.%(10Co/4Cr)/7(ZrO<sub>2</sub>-1.5 wt.% Y<sub>2</sub>O<sub>3</sub>) nanocomposite

WC/7 (10Co/4Cr))/7 ZrO<sub>2</sub> samples, respectively. The triangle indents located at the grain boundaries and inside the grains refer to the Berkovich indents developed upon examining the sample by nanoindentation. This approach was employed to study the degree of uniformity in the mechanical properties (hardness and Young's modulus) at the sub-microscale level. To tackle this task, more than 100 indents were developed for each composition, using the single-indent continuous multi-cycle ramp approach. The results showed that neither nanohardness nor Young's modulus varied dramatically from grain to grain (Fig. 11b, d), implying the absence of a serious compositional gradient at the microscale. The average values of nanohardness and Young's modulus obtained from at least 100 tests were found to be 19.67 and 275 GPa for the 93WC/7(10Co/4Cr) sample and 19.26 and 269 GPa for the 93(93-WC/7 (10Co/4Cr))/7 ZrO<sub>2</sub> sample, respectively.

Figure 12 shows the dependence of nanoindentations and nano-fracture toughness on the ZrO<sub>2</sub> content plotted for bulk nanocomposite 100-x(93-WC/7(10Co/4Cr)) /x ZrO<sub>2</sub> materials. The results show that increasing the ZrO<sub>2</sub> content leads to a slight decrease in the nanohardness, which decreased from 19.67 GPa (for # 93WC/7(10Co/4Cr)) to 19.26 GPa (for #

93(93-WC/7 (10Co/4Cr))/7 ZrO<sub>2</sub>. One can say that increasing the ZrO<sub>2</sub> content (x) may greatly improve the fracture toughness, as indicated by the monotonical increase in K<sub>C1</sub> with the increase in the ZrO<sub>2</sub> contents. A maximum of 15.48 MPa m<sup>1/2</sup> was achieved for 93(93-WC/7 (10Co/4Cr))/7 ZrO<sub>2</sub> bulk nanocomposite. This value is far higher than the one calculated for 93WC/7(10Co/4Cr), 8.83 MPa m<sup>1/2</sup>. We should emphasize that the addition of ZrO<sub>2</sub> nanograins increases the fracture toughness due to the transformation toughening (Ref 20, 21). It is believed that the polymorphic tetragonal-monoclinic phase transformation that occurs in ZrO<sub>2</sub> leads to a finite volume change (4-5%) and a large shear strain (14-15%) (Ref 22). The improvement taking place in the fracture toughness of the powder-mixture composites is believed to be caused mainly by the stress-induced transformation of the ZrO<sub>2</sub> phase as suggested by Miyazaki et al (Ref 23).

The coefficient of friction (COF), which is the ratio between friction force and the imposed normal force, was measured for bulk WC/7 wt.% (10Cr/4Cr)/7(ZrO<sub>2</sub>-1.5 mol.%Y<sub>2</sub>O<sub>3</sub>) nanocomposite sample, using pin-on-disk approach. The evolution of COF for 700 m of sliding distance is shown in Fig. 13. During the early stage of sliding distance (25 m), COF was 0.37. Increasing the sliding distance to 300 m led to decrease the COF to 0.29. During the last stage of the test (300-700 m), the COF saturated at 0.29-0.33, as shown in Fig. 13.

## 4. Conclusion

Nanocrystalline WC powders obtained after 20 h of ball milling were mechanically ball-milled with 7 wt.% of elemental (10Co/4Cr) powders, using a planetary-type ball mill with WC-milling tools. A metastable hcp-93WC/7(10Co/4Cr) solid-solution was obtained after 50 h of milling. Small weight fractions of (ZrO<sub>2</sub> + 1.5 wt.% Y<sub>2</sub>O<sub>3</sub>) powders on the hardness, fracture toughness and nanomechanical properties (nanohardness and Young's modulus) of WC/Co/Cr, the solid-solution-93WC/7(10Co/4Cr) powders were then mechanically mixed for 50 h with different compositions, x of (ZrO<sub>2</sub> + Y<sub>2</sub>O<sub>3</sub>) ranging between 0 and 7 wt.%, using the planetary-type ball mill. The as-ball-milled 93WC/7(10Co/4Cr) and 100-x(93WC/7(10Co/4Cr))/xZrO<sub>2</sub> nanocomposite powders were then consolidated in vacuum under a uniaxial pressure of 30 MPa at 1250 °C, using SPS technique. The fully dense nanocomposite bulk samples obtained via the SPS process maintained their nanocrystalline structure even after this consolidation step. The nanohardness and indentation fracture toughness (K<sub>c1</sub>) of the bulk consolidated materials decreased were investigated as a function of (ZrO<sub>2</sub> + 1.5 wt.% Y<sub>2</sub>O<sub>3</sub>) additives. The results of the nanoindentation test indicated that the consolidated samples over the entire range of ZrO<sub>2</sub> concentrations (0-7 wt.%) had low values for Young's modulus (297-318 GPa) due to their nanocrystalline structures. Moreover, the WC/7 wt.% (10Cr/4Cr)/7(ZrO<sub>2</sub>-1.5 mol.%Y<sub>2</sub>O<sub>3</sub>) showed excellent wear resistance, indexed by its low-value friction coefficient (~0.29).

## Acknowledgments

Appreciation is extended to the Kuwait Government through the Kuwait Institute for Scientific Research for purchasing all of the equipment used in the present work, using the budget dedicated

for the Project (P-KISR-06-04) led by the first author of Establishing Nanotechnology Center in KISR.

## References

1. J.S. Benjamin, Mechanical Alloying, *Sci. Am.*, 1976, **234**, p 40–49
2. C.C. Koch and Y.S. Cho, Nanocrystals by High Energy Ball Milling, *Nanostruct. Mater.*, 1992, **1**, p 207–212
3. M.S. El-Eskandarany, *Mechanical Alloying for Fabrication of Advanced Engineering Materials*, 2nd ed., Elsevier Inc, Philadelphia, PA, 2015 (19103-2899)
4. M.S. El-Eskandarany, Mechanical Solid State Mixing for Synthesizing of SiC<sub>p</sub>/Al Nanocomposites, *J. Alloys Comp.*, 1998, **279**, p 263–271
5. R. Md Raihanuzzaman, Z. Xie, S.J. Hong, and R. Ghomashchi, Powder Refinement, Consolidation and Mechanical Properties of Cemented Carbides—An Overview, *Powder Technol.*, 2014, **261**, p 1–13
6. R. Md Raihanuzzaman, S.-T. Han, R. Ghomashchi, H.-S. Kim, and S.-J. Hong, Conventional Sintering of WC with Nano-Sized Co binder: Characterization and Mechanical Behavior, *Int. J. Refract. Metal. Hard Mater.*, 2015, **53**, p 2–6
7. W. Su, Y. Sun, H. Wang, X. Zhang, and J. Ruan, Preparation and sintering of WC–Co composite powders for coarse grained WC–8Co hardmetals, *Int. J. Refract. Metal. Hard Mater.*, 2014, **45**, p 80–85
8. C. Suryanarayana and N. Al-Aqeeli, *Prog. Mater. Sci.*, 2013, **58**, p 383–410
9. D. Zheng, X. Li, X. Ai, C. Yang, and Y. Li, WC–Si<sub>3</sub>N<sub>4</sub> composites prepared by two-step spark plasma sintering, *Int. J. Refract. Metals Hard Mater.*, 2015, **50**, p 133–139
10. H. Engqvist, G.A. Botton, N. Axén, and S. Hogmark, A study of grain boundaries in a binderless cemented carbide, *Int. J. Refract. Metals Hard Mater.*, 1998, **16**, p 309–313
11. El-Eskandarany M. Sherif, Fabrication of nanocrystalline WC and nanocomposite WC–MgO refractory materials at room temperature, *J. Alloy Comp.*, 2000, **296**, p 175–182
12. M.S. El-Eskandarany, Top–down approach accompanied with mechanical solid-state mixing for producing nanocomposite WC/Al<sub>2</sub>O<sub>3</sub> materials, *Int. J. Nanopart.*, 2009, **2**, p 14–22
13. N. Ünal, F. Kern, M.L. Öveççü, and R. Gadow, Influence of WC particles on the microstructural and mechanical properties of 3 mol% Y<sub>2</sub>O<sub>3</sub> stabilized ZrO<sub>2</sub> matrix composites produced by hot pressing, *J. Eur. Ceram. Soc.*, 2011, **31**, p 2267–2275
14. S. Huang, K. Vanmeensel, O.V. Der Biest, and J. Vleugels, Sintering, thermal stability and mechanical properties of ZrO<sub>2</sub>–WC composites obtained by pulsed electric current sintering, *Front. Mater. Sci.*, 2011, **5**, p 50–56
15. Test Methods for Density and Specific Gravity (Relative Density) of Plastics by Displacement. ASTM Standard D792-00. Vol 81.01. American Society for Testing and Materials. West Conshohocken. PA
16. M.B. Raviathul, V.C. Srivastava, and N.K. Mukhopadhyay, Effect of milling time on structural evolution and mechanical properties of garnet reinforced EN AW6082 composites, *Metall. Mater. Trans. A*, 2014, doi:10.1007/s11661-014-2685-3
17. G.R. Anstis, P. Chantikul, B.R. Lawn, and D.B. Marshall, A critical evaluation of indentation techniques for measuring fracture toughness: I. Direct crack measurements, *J. Am. Ceram. Soc.*, 1981, **64**, p 533–540
18. M.T. Laugier, Surface toughening of ceramics, *J. Mater. Sci. Lett.*, 1986, **5**, p 252
19. M.T. Laugier, New formula for indentation toughness in ceramics, *J. Mater. Sci. Lett.*, 1987, **6**, p 355–356
20. T. Venkateswaran, D. Sakar, and B. Basu, Tribological properties of WC–ZrO<sub>2</sub> nanocomposites, *J. Am. Ceram. Soc.*, 2005, **88**, p 691–697
21. B. Basu, J. Vleugels, and O.V. der Biest, Processing and mechanical properties of ZrO<sub>2</sub>–TiB<sub>2</sub> composites, *J. Eur. Ceram. Soc.*, 2005, **25**, p 3629–3637
22. R.C. Garvie, R.H. Hannink, and R.T. Pascoe, Ceramic steel?, *Nature*, 1975, **258**, p 703–704
23. H. Miyazaki, Yoshizawa Yu-ichi, and K. Hirao, Effect of the volume ratio of zirconia and alumina on the mechanical properties of fibrous zirconia/alumina bi-phase composites prepared by co-extrusion, *J. Eur. Ceram. Soc.*, 2006, **26**, p 3539–3546